Validation of a Computational Approach to Predict Bursting Pressure of Scored Steel Plates

M. Colombo · P. Martinelli · M. di Prisco

Received: 3 September 2013 / Accepted: 19 June 2014

Introduction

In the last 20 years, a number of studies have examined the influence of boundary conditions, loading conditions and plate stiffeners in order to understand the deformation and tearing phenomenon of metallic plates [1, 2]. One of the most widely examined structural problems is that of a metallic circular plate, fully clamped and subjected to transverse im-pulsive loads [3].

M. Colombo · P. Martinelli (✉) · M. di Prisco
Department of Civil and Environmental Engineering, Politecnico di Milano, Milan, Italy
e-mail: paolo.martinelli@polimi.it

Although the behaviour of thin metallic circular plates has been extensively studied, the same is not true for thin metallic circular plates with grooves.

Thin circular scored plates are mainly used as safety device in equipment working under pressure (chemical plants, tanks, reactors, silos, etc.), often in conjunction with relief valves; if the pressure rises in a non-controlled way, equipment may be damaged or destroyed and personnel may be injured or killed. In case of overpressures, the use of these protective elements (often named rupture discs) provides an adequate fluid outlet, venting the pressure excess. The venting of the excessive pressure is guaranteed through the rupture of the disc with the formation of 4 or 6 petals.

Another important application of thin circular scored plates is as a critical device in shock tube facilities. Shock tubes are multipurpose experimental facilities, mainly used in aerodynamic investigations, whose basic layout consists of two rigid cylindrical chambers of equal cross-section, named high pressure and low-pressure, separated by a thin scored plate (diaphragm) [4]. Both the high-pressure (or driver) and the low-pressure (or driven) chambers contain gases whose initial conditions (pressure, temperature and molecular weight) at rest are different. The diaphragm rupture causes a rapid expansion of gas, ultimately resulting in a shock wave propagation moving into the driven section.

A third application of thin scored plates, not investigated in this study, is as a venting panel in case of blast; in this case the panels are used to reduce the pressure acting on the structure. In the first two situations the plates are essentially subjected to quasi-static loads, while in the latter case the plates are subjected to impulsive loads.

With reference to the first two situations, the distributed failure load (or burst pressure) and the opening process of thin scored plates have a relevant importance on the correct working of safety devices and on the performance of shock tube experiments, respectively.

For efficient shock tube operation, the rupture of the diaphragms has to be clean and instantaneous; it is desirable that metal diaphragms fail forming petals and that petals fold back against the shock tube walls so as not to hinder gas flow. As reported by Rothkopf and Low [5] and Hickman et al. [6], the imperfect burst of a shock tube diaphragm can significantly modify the flow field predicted by the ideal one-dimensional theory due to multi-dimensional disturbances.

A clean opening of the disc (in the following referred to as diaphragm) avoiding petal detachment is also desirable for correct working in the case of safety device application.

The aim of this study is the correct prediction of the diaphragm burst pressure as well as the actual reproduction of the plasticity and tearing phenomena which can significantly improve (a) performance in shock tube experiments and (b) the correct working of disc rupture.

The paper first describes the experimental tests carried out and the numerical model adopted to predict the diaphragm burst pressure. The capabilities and limits of the blind numerical results are then assessed through a comparison with measured experimental data. A numerical parametric study is carried out to better understand the diaphragm deformation mechanics and the influence of parameters on the diaphragms burst pressure. Finally, the need of the numerical procedure presented compared to classical design approaches is discussed.

Research Significance

The paper is aimed at presenting and validating a numerical procedure able to predict the burst pressure of scored plates often used as safety device or diaphragms in shock-tube facilities. In the first case a good prediction of the failure pressure allows the device to ensure safety in the case of overpressure; in the latter case, the reliable prediction of the burst pressure can improve shock-tube equipment performance and often also the repeatability of the shock pressure generated.

Experimental Tests

The experimental program presented herein is planned in order to establish the burst pressure and the structural response at failure of circular X-scored steel diaphragms with different thicknesses and score depths. Since one of the aims of the study is to predict the burst pressure of diaphragms used in shock tube facilities, the actual diaphragms loading conditions will be reproduced by performing the experimental program with part of the shock tube apparatus recently developed at the Politecnico di Milano by Colombo et al. [7].

Experimental Procedure

The diaphragms tested are placed at one end of a cylindrical chamber with a volume of 0.047 m^3 and a diameter of 481 mm. Each diaphragm is clamped between the pressurized chamber and a flange, tightened together by means of a set of twenty bolts closed through hydraulic nuts that ensure that the closing force is constant across the different bolts. The closing pressure applied by the bolts on the contact surface between the flanges is equal to 47 N/mm^2. The remaining end of the chamber is closed by a blind flange. Proper gaskets are used to ensure the sealing of the chamber. The scored face of each diaphragm is placed looking out from the loading chamber. A schematic view of the test set-up is provided in Fig. 1.

The pressurization of the chamber is accomplished by the introduction of helium; the use of helium instead of air has the advantage that there is no need for a compressor, since helium is normally contained in tanks at 200 bar. This means that a simple pressure reducer is sufficient to pressurize the chamber. The introduction of helium inside the chamber is controlled by an electro-valve connected to a remote PC that stops the introduction of helium just after the bursting of the diaphragm. The resulting pressure time history is linear with an average loading rate of about 0.0135 MPa/s.

During the test, the pressure inside the pressurized chamber is monitored and recorded through static and dynamic pressure transducers, both mounted on the external surface of the chamber.

Diaphragm Geometry and Material

The diaphragms used in this study have the same geometry and are made of the same material of those normally adopted during shock tube tests. The diaphragms have a circular shape with a diameter of 697 mm, and are obtained by laser cutting from hot rolled sheets of different thicknesses. The diaphragms are loaded by a uniform pressure maintained over a circular area, the diameter of which corresponds to the internal pressurized chamber size (481 mm). On the surface of the diaphragm not in contact with the pressurized gas, two grooves are scored which cross the centre of the diaphragms. The two grooves are inclined at 90° with respect to each other. The geometry of diaphragms, the grooves and the loaded area are shown in Fig. 2.

In this study, two different typologies of diaphragms are examined: they differ in thickness and score depth (Table 1). The 4 and 2 mm thick diaphragms have a tolerance on the thickness respectively equal to ± 0.18 mm and ± 0.14 mm. The two typologies, in the following indicated as types A and B, correspond to decreasing levels of burst pressure. The range of burst pressures examined in this study varies from about 2.5 MPa to 1.0 MPa.

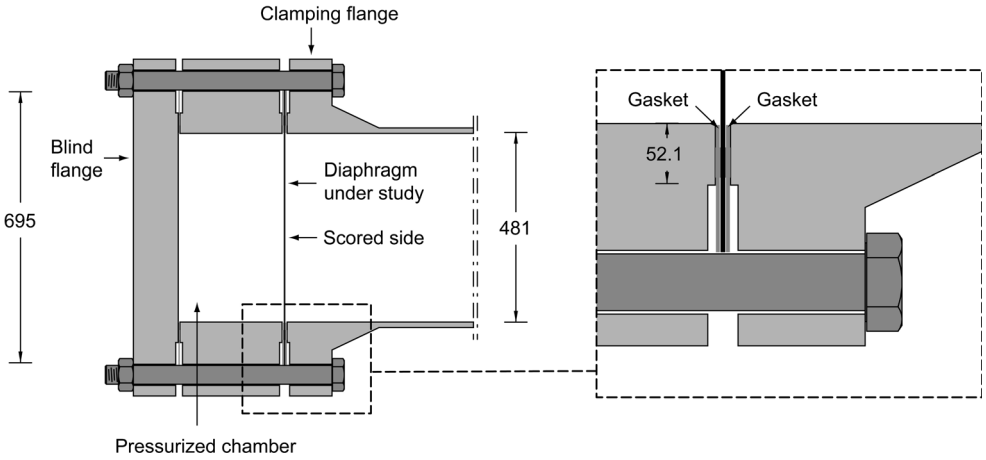

Fig. 1 Schematic view of the experimental test set-up (units mm)

Grooves are obtained through a milling machine on which an end mill cutter with 4-teeth is mounted, with a diameter of 5 mm, a helix angle of 30° and a coating made in titanium aluminium nitride (TiAlN). The machining is performed by setting the ligament (plate net thickness in the groove) as constant independently from the sheet thickness tolerance. A view of the groove cross-sections obtained with microscopy with an enlargement of 10 times is shown in Fig. 3 for the two diaphragm typologies. The main geometrical characteristics of the two diaphragm typologies used in this work are summarised in Table 1.

All diaphragms tested in this study are made of S235 JR structural steel in accordance with UNI EN 10025-2 [8]. This material choice is motivated by the fact that steel can guarantee burst pressure in the range of interest with a small thickness. In addition, S235 JR steel is easily available and inexpensive. For each diaphragm typology, a small specimen with the same thickness of the diaphragms is extracted from the same plate used to obtain the diaphragms. The specimens, with a length of 300 mm and a width of 20 mm, are tested in uniaxial tension following the standard tensile tests described in UNI EN ISO 6892-1 [9]. The nominal stress-nominal strain curves obtained from the test results on the two small specimens are shown in Fig. 4(a). The notation used to indicate the small specimens is equal to that adopted to indicate the diaphragms (types A and B).

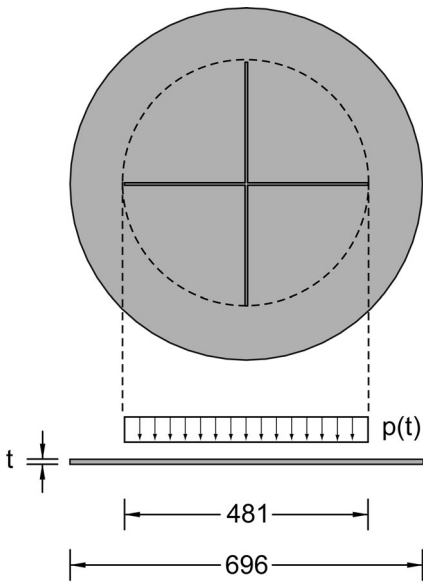

Fig. 2 Diaphragm geometry and loaded area (units mm)

Instrumentation and Test Program

A set of two pressure transducers is used to measure the pressure evolution during the tests. The first pressure transducer is a static pressure transducer with a full scale pressure of 6.9 MPa, with an accuracy equal to 0.5 % of the full scale and a response time shorter than 0.5 ms. The second pressure transducer is an ICP (Integrate Circuit Piezoelectric) dynamic transducer made of a quartz sensing element with a full scale pressure of 6.9 MPa, a sensitivity of 0.7 mV/kPa, a rise time lower than 1 μs and a resonant frequency higher than 500 kHz (PCB M102B04).

In order to better understand the diaphragms structural behaviour and to validate the numerical models, four strain gauges are mounted on the diaphragm surfaces. The first two strain gauges (SG1 and SG2) are placed on the scored side of the diaphragms in proximity to the intersection of the grooves (Fig. 5(a)). The two strain gauges are placed along the axes of symmetry, SG1 along the radial direction (or x-direction with reference to Fig. 5(a)) while SG2 is placed along the orthogonal direction with respect to the previous one (or the y-direction with reference to Fig. 5(a)). The third and fourth strain gauges (SG3 and SG4) are mounted on the non-scored diaphragm side. SG3 is placed along the x-symmetry axis, but quite far from the intersection of the grooves (Fig. 5(b)). Finally, strain gauge SG4 is mounted across one groove in order to eventually capture the tear propagation. The exact location of all strain gauge barycentres is detailed in Fig. 5,

Table 1 Geometric characteristics of the diaphragms investigated

Diaphragm types	Thickness [mm]	Score depth [mm]	Score width [mm]	Score corner radii [mm]	Score depth—thickness—ratio
A	4	1.6	5.0	0.25	0.4
B	2	0.8	5.0	0.25	0.4

while a picture of a completely instrumented diaphragm ready to be tested is shown in Fig. 6.

Strain gauges have a nominal resistance of 120 Ω and a gauge length of 3 mm. The strain gauge signal is conditioned by a transducer amplifier with gain varying between one and 5000, with 0.05 % resolution, 100 kHz bandwidth and a broadband electrical noise equal to 0.3 μV rms (root mean square). All channels are acquired by means of the same data acquisition with a 14 bit resolution at a sampling rate of 1.5 kS/s per channel.

Since the instruments SG3 and SG4 are loaded by the pressure in the direction perpendicular to the strain-gauge grid plane, another strain-gauge (SG5), free standing in the chamber and not connected to any element, is introduced inside the pressurized chamber during each test in order to measure the influence of the pressure on the strain measurements.

Being ε_l the longitudinal strain parallel to the strain-gauge grid, ε_t the transverse strain with respect to the grid direction, the strain indicated by the strain gauge (ε') can be defined as follows [10, 11]:

$$\varepsilon' = \frac{\varepsilon_l + S_t \varepsilon_t}{1 - \upsilon_0 S_t} + \varepsilon_\perp(p) \tag{1}$$

where S_t is the transverse sensitivity of the instruments, ν_0 is the steel Poisson coefficient and $\varepsilon_\perp(p)$ is the strain read by the instrument when a pressure p is applied perpendicularly to the grid plane. This strain is related to the pressure sensitivity of the strain gauge.

Since the transverse sensitivity of the strain gauge used is negligible (0.2 %), the longitudinal strain ε_l that we intend to measure can be written as:

$$\varepsilon_l = \varepsilon' - \varepsilon_\perp(p) \tag{2}$$

The measurements of SG5 are used to define a function for $\varepsilon_\perp(p)$ that is chosen as non-linear and described by the following equations:

$$\begin{cases} \varepsilon_\perp(p) = \left(0.7454p^3 - 2.6687p^2 + 3.2687p - 0.019\right)\cdot 10^{-4} & p < 1.3 \text{ MPa} \\ \varepsilon_\perp(p) = 1.3579\cdot 10^{-4} & p > 1.3 \text{ MPa} \end{cases} \tag{3}$$

A comparison between the chosen function and the experimental results is represented in Fig. 7.

In the case of SG1 and SG2, since no pressure is applied perpendicular to the grid plane and the instrument transverse sensitivity is once again negligible, the measurements read can be assumed corresponding to the longitudinal strain.

The strain gauge wires have to pass from the pressurized chamber, which is assembled with two other flanges in order to guarantee a perfect seal, to the external data acquisition system without being damaged. Even if a particularly careful procedure is used to protect the wires which connect the strain gauges to the data acquisition system, some signals are lost due to the damage of the wires themselves.

A total of six scored diaphragms are tested following the procedure described in Experimental Procedure sect.: three diaphragms of type A and three diaphragms of type B (see Table 1 for the main geometric characteristics). To indicate to which diaphragm we are referring, a progressive number will

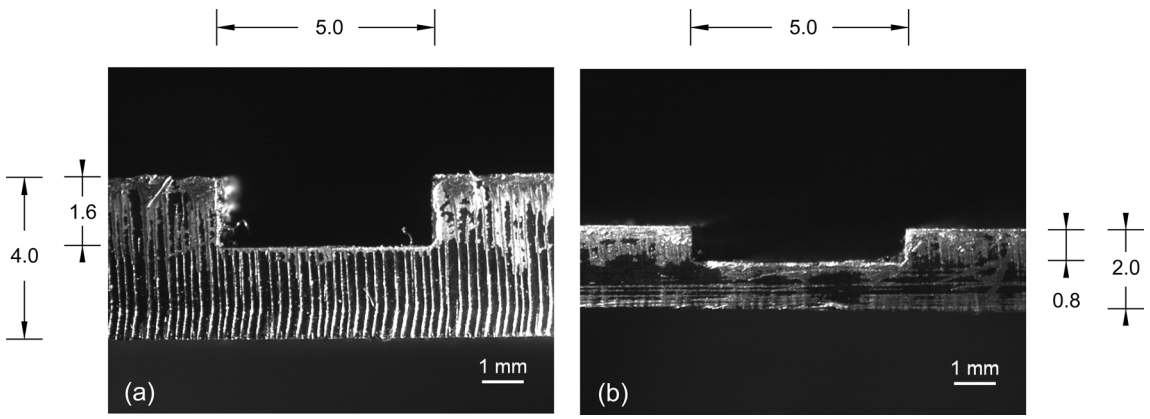

Fig. 3 Groove cross-sections for (**a**) diaphragms of type A and (**b**) diaphragms of type B (units mm)

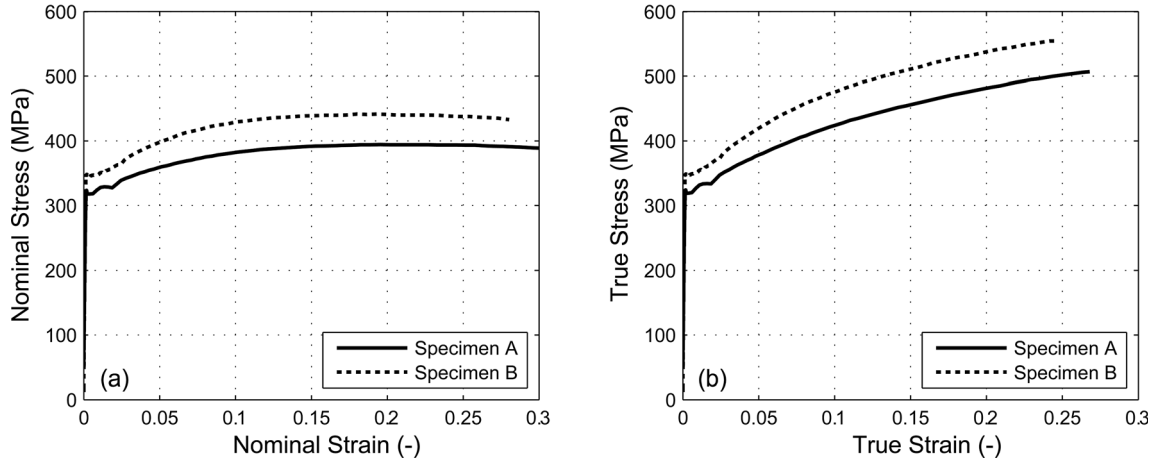

Fig. 4 Uniaxial tensile curves: (**a**) nominal stress-nominal strain and (**b**) true stress-true strain

be associated to the typology of the diaphragms (A, and B), which results in A1, A2, A3, B1, B2 and B3.

Finite Element Models

Different finite element models for each thickness–score depth couple are developed to predict and simulate the behaviour and the burst pressure of scored steel diaphragms. Models are three-dimensional and geometric nonlinearity is taken into account by adopting a large deformation assumption. Large deformation effects are accounted for by a finite-strain formulation based on an update Lagrangian approach for the solid eight-node elements which are formulated in the current configuration using current nodal positions.

Although the problem under study is essentially static before the tearing propagation, explicit dynamic analysis is conducted in order to capture the actual behaviour of the diaphragms. An explicit time integration scheme is preferred to implicit and static analysis for the expected high nonlinearity connected to the petals formation. The explicit dynamic analyses are carried out based on the central difference integration rule, with dynamic equilibrium equations satisfied at the beginning of the time increment Δt.

All numerical simulations reported in Experimental vs Numerical Results sect. are performed using the finite element program ABAQUS/Explicit 6.7 which allows the automatic estimation of a stable time increment [12].

Whilst the explict dynamic procedure is applied to quasi-static problems, as in the one investigated, some special considerations are necessary on the total time duration of the analyses. In particular the time scale has to be shortened (or equivalently the event accelerated), in order to obtain an economic solution [12].

The method adopted in this study to accelerate the physical process is to increase the loading rate so that the process occurs in a shorter time; whilst at the same time the dynamic

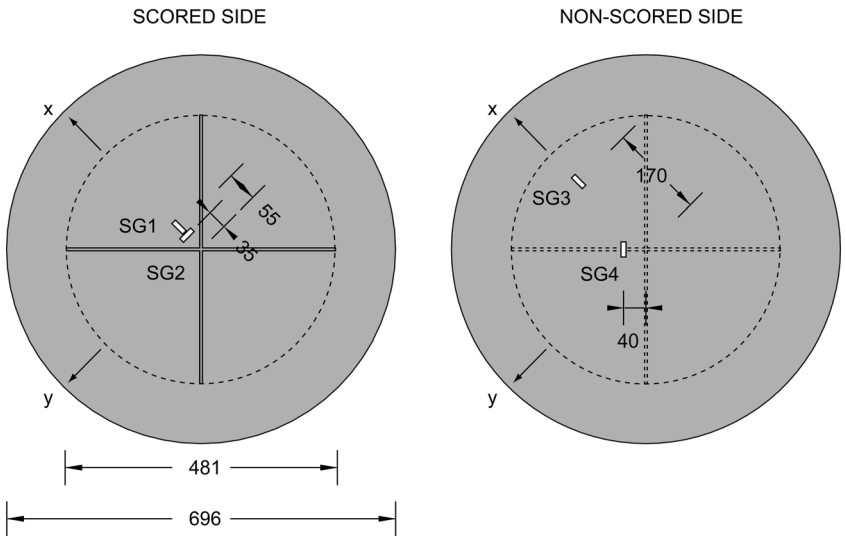

Fig. 5 Location of strain gauges on the diaphragms (units mm)

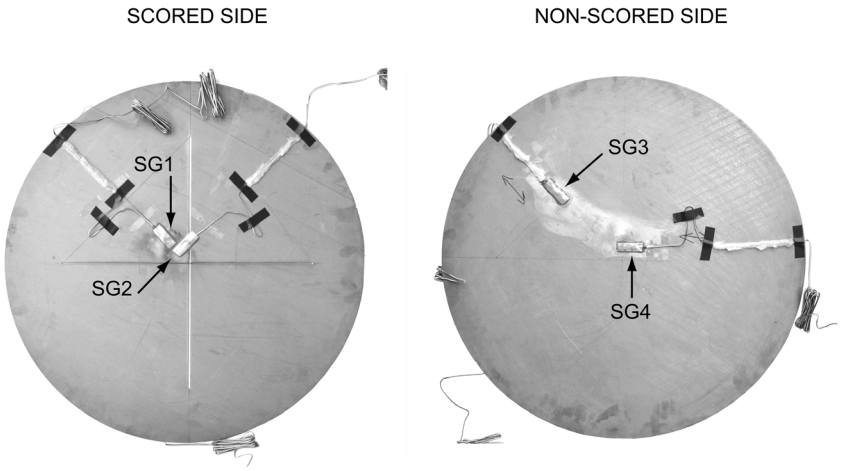

Fig. 6 Photograph of an instrumented specimen ready to be tested

effects must be checked in order to remain insignificant. The time required to obtain the static response is deduced from the frequency of the lowest mode which usually controls the response of the structure in a static analysis. As reported by Baker et al. [13], for an undamped perfectly elastic system the quasi-static loading regime is valid for:

$$\omega \cdot t_d > 40 \tag{4}$$

where ω is the fundamental frequency and t_d is the total time load duration. The total time duration t_{tot} of the analyses is deduced from equation (4) and it is equal to:

$$t_{tot} = \frac{40}{\omega_1} \tag{5}$$

where ω_1 is the lowest mode frequency in the numerical model.

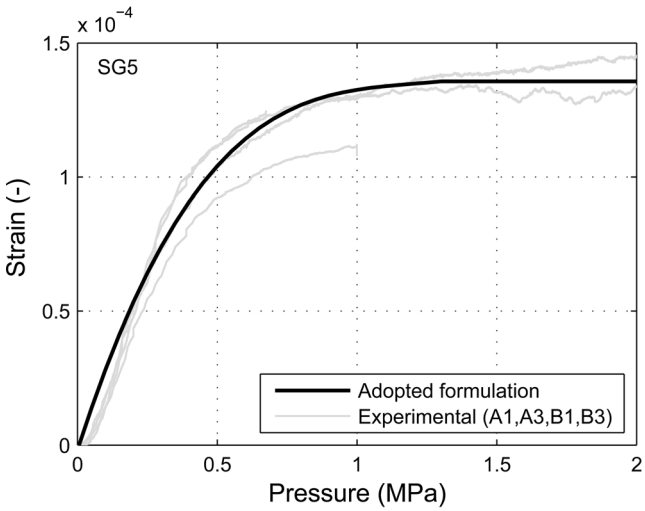

Fig. 7 Strain gauge sensitivity to the applied pressure

Geometric Modelling

Eight-node reduced integration and hourglass control brick elements (C3D8R) with three degrees of freedom per node are employed to discretise the diaphragms. Due to symmetry, it is sufficient to model a quarter of each scored diaphragm. Symmetrical boundaries are imposed on the *x-z* and *y-z* planes. According to the experimental set-up used, the diaphragms investigated behave as fully fixed along a circumference that has a diameter equal to the internal diameter of the pressurized chamber (see Fig. 1). Figure 8(a) illustrates the boundary conditions assumed and a mesh plan view; a frontal view zoom at the grooves intersection is shown in Fig. 8(b). Asymmetric tearing of the diaphragms cannot be predicted due to the assumed symmetry in the model.

The structured mesh technique is not applicable to almost all regions of the one quarter circular plate with groove, then a swept meshing technique with advancing front algorithm is used in this study [12].

In order to guarantee that the model predictions are unaffected by the mesh resolution, a mesh convergence study is carried out. Three mesh resolutions for each diaphragm typology are considered by increasing the number of elements along the thickness (Table 2). The number of elements along the thickness is varied: 4, 6 and 8 elements are considered for diaphragm type A while 2, 4 and 6 elements for diaphragm type B. With the increasing of the number of element along the thickness, the three corresponding models are labelled as "Basic", "1° Refinement" and "2° Refinement". In the same table, the average element aspect ratio as well as the percentage of elements with an aspect ratio larger than 10 are indicated in order to better appreciate the mesh quality.

Global responses (central displacement evolution vs increasing pressure) obtained with the three different mesh resolutions are compared: basically no difference is found for both diaphragm typologies (Fig. 9). Just a small difference is found in the global response during the petal formation phase. This difference is mainly related to the regularization

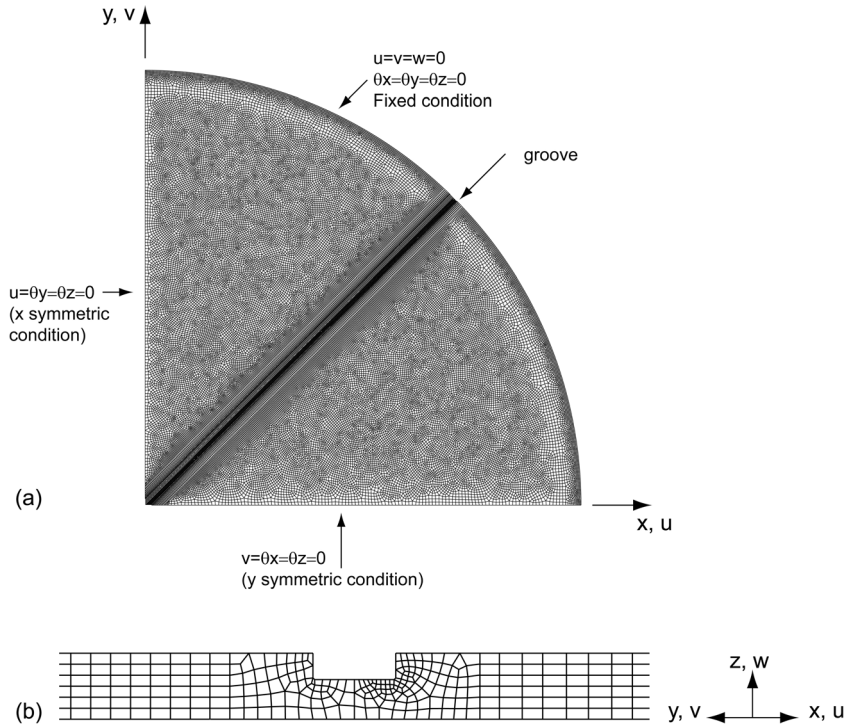

Fig. 8 (**a**) Boundary conditions on the quarter model of the diaphragm and (**b**) zoom at the grooves intersection

process of crack propagation and not to mesh convergence. In the case of diaphragm type A, starting from the "1° Refinement" mesh, a fourth mesh (labelled in Table 2 as "3° Refinement"), characterized by the same number of elements on the thickness, but with lower element aspect ratio is considered. Even if global response of this mesh is identical to those previously presented (Fig. 9), it is adopted since we are interested in comparing experimental and numerical local response in terms of strain. The meshes used in the subsequent numerical analyses are indicated in bold in Table 2.

The oscillations visible in Fig. 9 are small perturbations due to the adoption of a dynamic FE solver for a quasi-static problem; in fact, the use of a static solver would not show such oscillations. Nevertheless, a static algorithm would not allow to represent the petals formation (high nonlinear phenomenon) necessary for the bursting pressure estimation as instead a dynamic explicit scheme is able to capture. These oscillations are almost absent for type A diaphragm since it is able to manifest a higher dumping, thanks to its higher thickness.

Material Modelling

The nominal stress—strain curves obtained from tensile tests described in Diaphragm Geometry and Material sect. (Fig. 4(a)) are converted into true stress—true strain curves (Fig. 4(b)) according to the following relationships:

$$\varepsilon = \ln(1 + \varepsilon_{nom}) \tag{6}$$

$$\sigma = \sigma_{nom}(1 + \varepsilon_{nom}) \tag{7}$$

where ε_{nom} and σ_{nom} are the nominal strain and stress [12]. An elasto-J2 plastic material model with isotropic hardening, a Young's modulus E=210,000 N/mm^2 and a Poisson's ratio ν=0.3 is assumed in the analyses.

Table 2 Summary of the finite element mesh characteristics; the labelled solutions correspond to the adopted ones (A.R. = aspect ratio)

Diaphragm types	Mesh density	Elements on thickness	Elements	Nodes	Average A.R.	A.R. > 10 [%]
A	Basic	4	114640	142624	3.2	4.0
A	1° Refinement	6	126194	148922	4.0	3.3
A	2° Refinement	8	177005	201832	4.8	1.9
A	**3° Refinement**	**6**	**301644**	**355288**	**1.7**	**0.0**
B	Basic	2	54950	79895	4.1	6.2
B	**1° Refinement**	**4**	**108376**	**138898**	**2.8**	**0.2**
B	2° Refinement	6	213812	252894	5.0	5.0

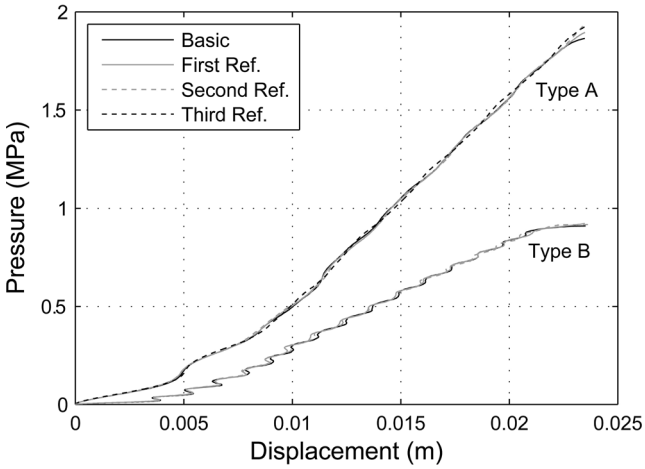

Fig. 9 Global results (numerical pressure vs central displacement) with different mesh refinements for diaphragms types A and B

In conjunction with the J2 plasticity model, a ductile progressive failure criterion is adopted to reproduce the actual behaviour of the diaphragms. The damage initiation indicator used in this study is that proposed by Hancock and Mackenzie [14] in the integral form introduced by Gunawardena et al. [15]. The Hancock-Mackenzie damage initiation indicator has a micromechanical foundation in which voids and defects grow; the void growth is reasonable if at least one principal stress component is tensile and this represents the applicability limit of the damage indicator [14]. The equivalent plastic strain to fracture ε_f relates the critical strain ε_0 of a uniaxial case to triaxial case and is given as in Fischer et al. [16]:

$$\varepsilon_f = 1.65 \cdot \varepsilon_0 \cdot \exp\left(-\frac{3}{2} \cdot \frac{\sigma_H}{\sigma_{eq}}\right) \tag{8}$$

The parameter ε_0 is a material parameter that can be determined by an instrumented tension test, σ_H denotes the hydrostatic (mean) stress, σ_{eq} is the von Mises equivalent stress while the ratio σ_H / σ_{eq} is known as stress triaxiality. Critical strain ε_0 corresponds in uniaxial tension to the onset of unstable crack propagation. The complete treatment of the calibration of this parameter is provided by Fischer et al. [16]; in this work the parameter ε_0 is set equal to 0.75 as proposed by Wasicek et al. [17] for similar structural steels.

The damage initiation indicator used is defined as:

$$D_i = \int_0^{\varepsilon_{eq}} \frac{d\varepsilon_{eq}}{\varepsilon_f} = \frac{1}{1.65\varepsilon_0} \int_0^{\varepsilon_{eq}} \exp\left(\frac{3}{2} \cdot \frac{\sigma_H}{\sigma_{eq}}\right) d\varepsilon_{eq} \tag{9}$$

where ε_{eq} is the accumulated equivalent plastic strain defined as:

$$\varepsilon_{eq} = \int_0^t \sqrt{\frac{2}{3} \dot{\varepsilon}_{ij}^{p} \dot{\varepsilon}_{ij}^{p}} d\tau \tag{10}$$

and $\dot{\varepsilon}_{ij}^{p}$ vector. The damage initiation indicator D_i is a state variable that increases monotonically with plastic deformation and damage initiation is met when D_i reaches unity. Once the damage initiation criterion is satisfied, damage evolution occurs. In order to reproduce an instantaneous failure once the damage initiation indicator D_i reaches unit, a plastic displacement value at failure close to zero is set (5×10^{-4} mm), since a zero value is not recommended [12]. A plastic displacement-based linear damage evolution law is used for the numerical simulations. Once damage is equal to one the elements are removed from the mesh allowing the tear formation and propagation to be simulated.

Experimental vs Numerical Results

In this section the results of the experimental tests are presented and the quality of the numerical results is assessed through comparison with the experimental data. In order to better identify the benefits and limitations of the modelling strategies, the numerical results are derived under blind prediction conditions, which means that the numerical results are obtained without the knowledge of the measured experimental response.

The quality assessment of the numerical predictions is first of all based on the burst diaphragm pressure. The burst pressure in the numerical simulations corresponds to the pressure that initiates the first tear formation along the grooves. Together with the loading rate, Table 3 reports the experimental burst pressures for each test; for the same diaphragm typology, the average experimental burst pressure is reported. The average values are compared with the numerical values and the percentage errors, reported in Table 3, permit a quick assessment of the numerical prediction accuracy. The agreement between experimental and numerical burst pressure values is particularly good for both diaphragm types A and B, with percentage errors of −12.4 % and −8.2 % respectively. The decrease in the burst pressure passing from type A to type B is evident and corresponds to a reduction of about a factor of two. It is worth noting that this factor is equal to the ratio between the ligament heights of the two diaphragms investigated. This means that the bursting process is governed by the membrane behaviour of the diaphragms, since large deflections at failure are reached. The numerical investigations also confirm this assumption: as a matter of fact, both the principal strains in the deformed mid-plane of the specimen at failure (ε_I and ε_{II}) are found to be positive (i.e. tension); the third principal strain ε_{III} is perpendicular to the deformed mid-plane.

The deformed configuration at failure for the three diaphragms type A is shown in Fig. 10. The diaphragms show similar deformations at failure, all characterised by a single

Table 3 Burst pressure values from test measurements and numerical analysis

Specimen	Experimental			Numerical	Error
	Loading rate [MPa/s]	Burst pressure [MPa]	Average burst pressure [MPa]	Burst pressure [MPa]	[%]
A1	0.0164	2.42	2.26	1.98	−12.4
A2	0.0117	2.11			
A3	0.0121	2.25			
B1	0.0140	1.00	1.01	0.93	−8.2
B2	0.0132	1.15			
B3	0.0131	0.89			

tear along one groove direction without the formation of petals. Figure 11 illustrates the deformed configuration at failure for type B diaphragms: in two diaphragms over three (Fig. 11(a, c)) complete petal formation is observed (four petals) which corresponds to a large portion subjected to tearing. For the third diaphragm (Fig. 11(b)) tearing completely occurred along one groove direction and partially along the orthogonal groove direction; this corresponds to the formation of two over four petals. On the same diaphragm a partial tearing along the circumferential clamped edge can be observed.

The two diaphragms experience a symmetric and an asymmetric failure mechanism respectively for type B and A. The latter is associated to a more unstable tearing propagation while the higher stability of the former guarantees stress redistribution and therefore the formation of two different tearings. The larger thickness may correspond to a larger number of defects in the ligament section, thus leading to an increase of the asymmetry of the diaphragm failure mechanism. Moreover, the comparison between the energies developed in the two different diaphragm types may help to understand the different failures. Since the failure mechanism, in both cases, is governed by a membrane behaviour, the energy dissipated in the tearing formation is linear with the thickness and therefore is double for type A diaphragm with respect to type B one. On the other hand, the numerical simulations show that the elastic energy (*SE*) released at the tearing onset for the case of type A diaphragm is 3.2 times larger than that released in type B diaphragm (elastic released energy: SE_A= 48 J, SE_B=15 J). This means that, since the ratio between released and dissipated energy is larger for type A diaphragm, it experiences a more unstable tearing propagation that may lead to the formation of just one tearing (asymmetric failure). The same conclusion can be drawn looking at the maximum equivalent plastic strains experienced at failure by the two different diaphragms (Figs. 14(c) and 15(c)): the type A shows a smaller plastic strain that means a more unstable tearing propagation process.

Figures 12 and 13 show the numerical displacement evolution of the diaphragm central node under increasing pressure levels, for diaphragms of type A and B respectively. In these figures, the slope change in the curves corresponds to a transition from plate to membrane diaphragms behaviour. At points PA3 and PB3 (Figs. 12 and 13) high values of equivalent plastic strains are reached in the diaphragms, corresponding to about 35 % and 40 % of the critical strain ε_0. Points PA1 (PB1) and PA2 (PB2) correspond to equivalent plastic strains respectively smaller than 1 % (<1 %) and equal to 13 % (7 %) of the critical strain ε_0.

The accumulated equivalent plastic strains for the three aforementioned different levels of applied pressure are depicted in Figs. 14 and 15 for type A and B diaphragms. In

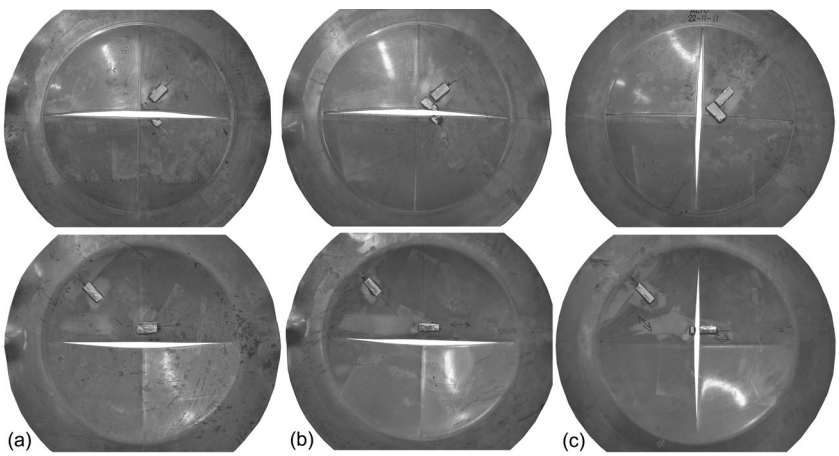

Fig. 10 Photographs of deformed shapes at failure for diaphragms of type A: (**a**) test A1, (**b**) test A2 and (**c**) test A3

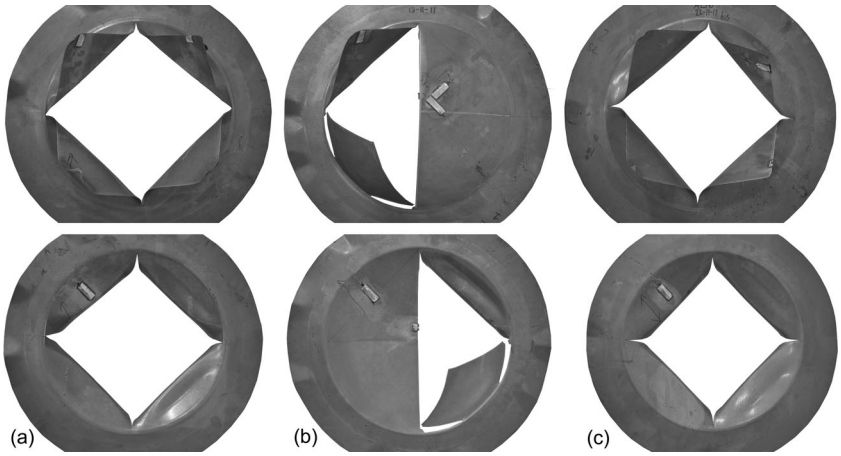

Fig. 11 Photographs of deformed shapes at failure for diaphragms of type B: (**a**) test B1, (**b**) test B2 and (**c**) test B3

these figures, a plane view (scored side) and a view close to the grooves intersection is given. At low levels of applied pressure the plasticity is concentrated along the grooves, especially in the central part of the diaphragms (Figs. 14(a) and 15(a)). For pressure of about 1/2 of the failure burst pressure, plasticity has completely developed along the grooves, and also in the region along the clamped edge (Figs. 14(b) and 15(b)). Looking at the same figures it can be observed as plasticity phenomena interest only the scored region (Fig. 15(b)) and marginally the region outside the grooves (Fig. 14(b)). Finally, for a pressure close to the burst pressure, plastic dissipation has completely spread in the not scored region. In the same figures, the plastic strain growth along the thickness at the grooves intersection is also evident. It is possible to observe as at low levels of applied pressure, which correspond to small plastic strain values, there is an asymmetrical distribution of equivalent plastic strains at the grooves intersection (Figs. 14(a) and 15(a)) that is due to a light mesh asymmetry (see Fig. 8(b)). As the applied pressure increases, the stress redistribution favours a more symmetric distribution of the equivalent plastic strains.

Numerical results confirm that tearing occurs propagating from the central region of the diaphragm, in particular at the intersection of the grooves, toward the fixed edges. This behaviour is clearly confirmed by Figs. 16 and 17, which show the damage initiation indicator contour (D_i) at failure for types A and B diaphragm, respectively; the maximum damage indicator value is localised close to the intersection of the grooves. In the same figures, the numerical tearing of the plate at the grooves intersection is evidenced and compared with the experimental one: the irregular profile of the tearing can be observed both numerically and experimentally.

The good agreement between experimental and numerical burst pressure confirms the accuracy of the numerical model in the reproduction of the global response. The comparison is also extended to the determination of the local response, by evaluating the strain evolution as a function of the applied pressure at four different locations, namely SG1, SG2, SG3 and SG4 (Fig. 5). These quantities are shown respectively in Figs. 18, 19, 20 and 21 for type A and in Figs. 22, 23, 24 and 25 for type B diaphragms; a solid black line is used for the experimental values while a solid grey line for the numerical

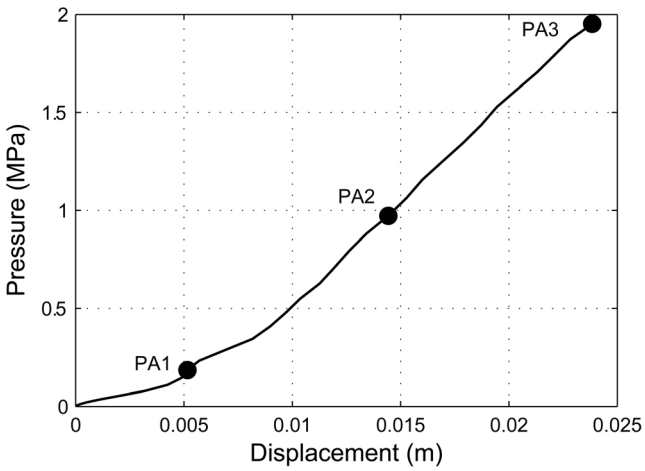

Fig. 12 Numerical pressure vs central displacement for diaphragms of type A

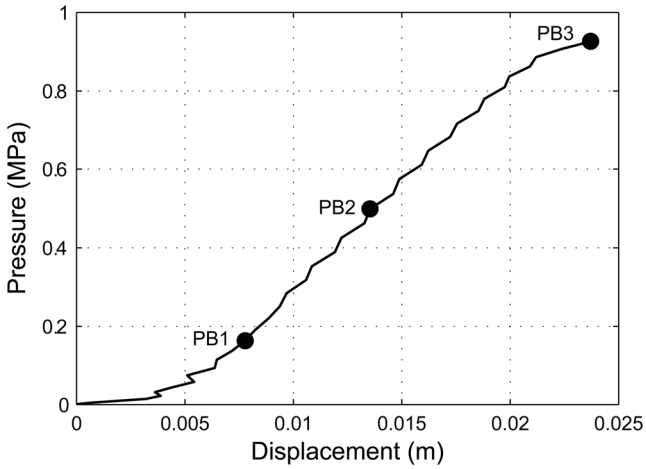

Fig. 13 Numerical pressure vs central displacement for diaphragms of type B

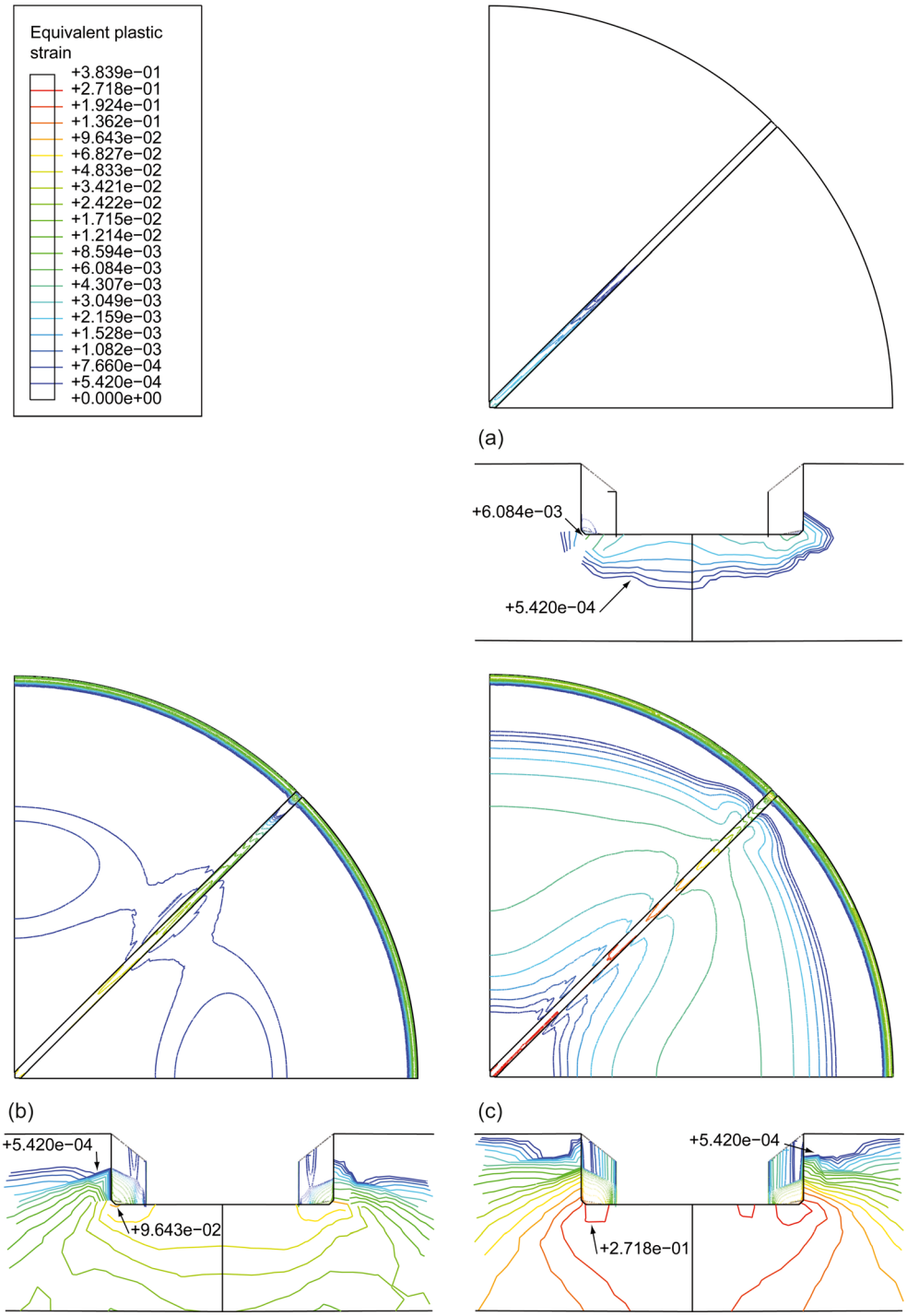

Fig. 14 Equivalent plastic strain evolution for diaphragms of type A: (**a**) point PA1, (**b**) point PA2 and (**c**) point PA3 in Fig. 12

ones. The fitting of experimental strains provided by numerical analyses is quite remarkable for SG1 and SG4 in the case of type A diaphragm (Figs. 18 and 21) and for SG1, SG2 and SG4 in the case of type B diaphragm (Figs. 22, 23 and 25), while the SG3 gauge measures are overestimated for both diaphragm typologies.

For type A diaphragms, the difference between numerical and experimental response (see Figs. 19 and 20) can be caused by asymmetry induced by geometric tolerances and defects distribution inside the material. On the other hand, the numerical model imposes geometrical symmetry of the diaphragm (one-quarter model) and adopts a homogeneous material, neglecting geometric and mechanical defects; the only source of asymmetry is in the mesh that just causes a local effect in plastic strain distribution as discussed before.

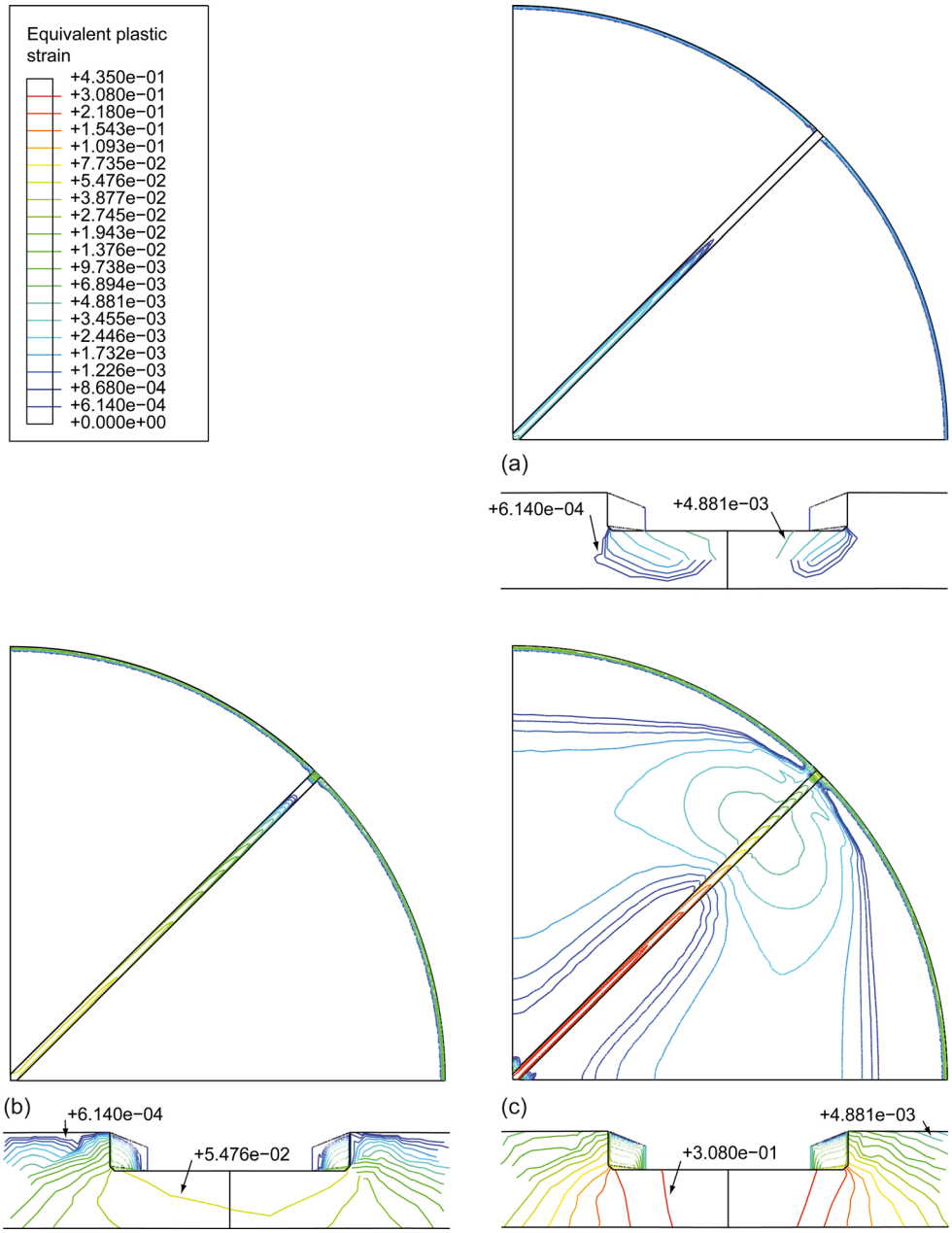

Fig. 15 Equivalent plastic strain evolution for diaphragms of type B: (**a**) point PB1, (**b**) point PB2 and (**c**) point PB3 in Fig. 13

The behaviour of SG1 and SG2 strains for both types of diaphragms (Figs. 18, 19, 22 and 23) is characterized by positive (tension) value for all pressure range and by a marked slope change at a relative low pressure values. In fact, strain gauges SG1 and SG2 are placed on the scored side of the diaphragm in proximity of the grooves intersection that always results in tensile values. The first change of slope indicates a transition from a plate to a membrane behaviour similarly to what observed for the central displacement.

The strain gauge SG2 is placed close to the centre on a tensile strip that connects two grooves with an orientation to 45° with respect to the grooves. The extremities of this strip are more deformable with respect to the central part (SG2 gauge) due the presence of the grooves. When the strip ends yield, the internal region unload in order to respect the compatibility fixed by the distance of the two grooves (Fig. 19). The FE model is characterized by a higher stiffness and is thus less sensible to this phenomenon.

The SG3 gauges behaviour is characterized by an ascending branch followed by a descending one (Fig. 20) or by a plateau (Fig. 24). The strain SG3 is initially in tension because it is placed close to the clamped edge on the non-scored diaphragm side. The numerical strain distribution along the thickness, at the SG3 gauge location, explains the experimental behaviour recorded: it evolves from a tension to compression distribution, moving from non-scored to scored sides, to a

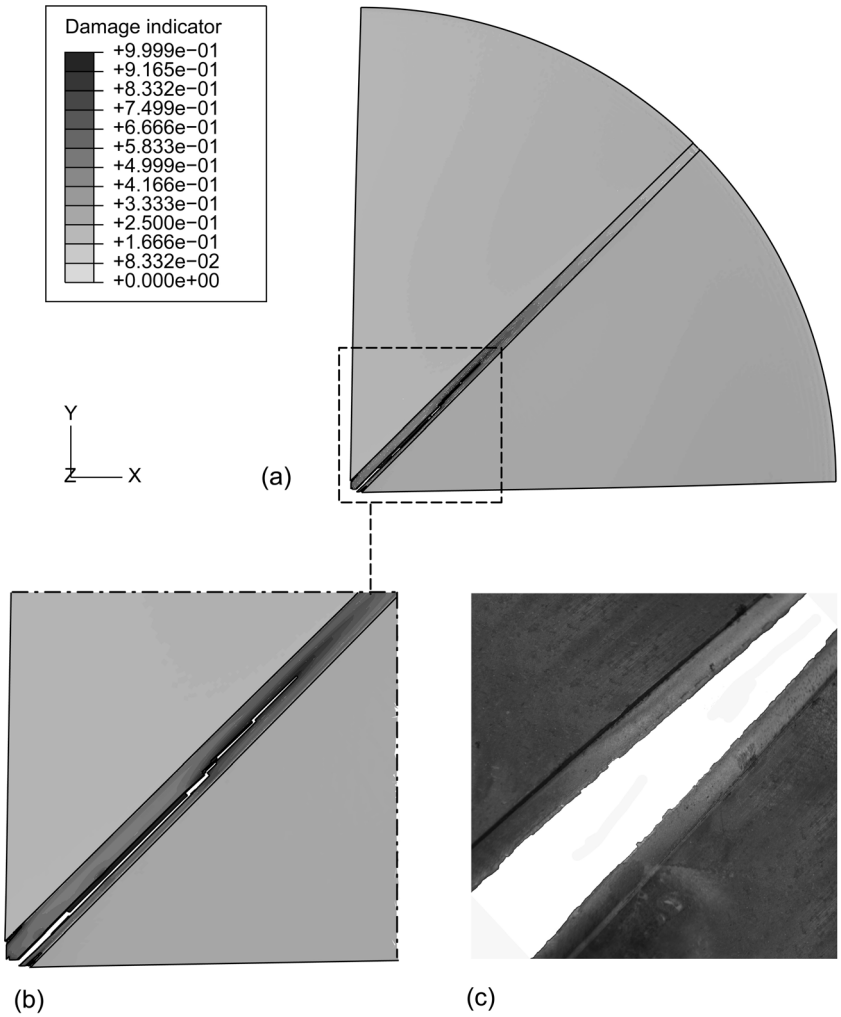

Fig. 16 Damage initiation indicator computed in diaphragm type A during tearing formation (**a**–**b**) and zoom at failure for diaphragm A2 (**c**)

tension-tension distribution when, at failure, the scored side values are one order of magnitude higher than the non-scored one. In type A diaphragm the second change of slope in the experimental results is related to a local bending phenomenon (see Figs. 10(b) and 20). The difference between the numerical and experimental strain results for type B SG3 is caused by the location of the experimental yield line that arises in a different position with respect to the strain gauge (see Figs. 11(a) and 24).

The numerical results show the formation of yield line along the clamping edge (see Fig. 15) and are characterized by a spreading of the plastic strain in the surrounding region. On the other hand the experimental tests for type B diaphragms clearly show a yield line far from the clamping edge, more internal with respect to the SG3 location and characterized by a strain localization (see Fig. 11). These two observations explain the experimental SG3 low value and the higher numerical value both lower than the yield strain.

The difference between the experimental and numerical SG3 results and more in general between the yield line different positions could be due to the simplification introduced in the FE model for the description of the boundary condition. In particular, the FE model assumes a perfect fixed condition along the tube internal diameter (see Fig. 8), while the experimental set-up, even if conceived to reproduce a perfect clamping, is more complex (presence of the gasket, not infinity clamping force, angles not at 90° between the two chambers) and is not able to perfectly reproduce a clamping condition.

Figures 21 and 25 show the numerical and experimental SG4 measures comparison. It is worth remembering that strain gauges SG4 are placed across the groove: their rupture due to the tearing phenomenon justifies the vertical asymptote in the experimental data. In the same figures it is possible to observe that SG4 is initially in compression, being it placed in the central part of the non-scored diaphragm side; as the pressure increases, the strain in compression increases until reaching a maximum point (minimum point in the figures). After this point, an increase of the applied pressure corresponds to a monotonic increase of strain from compression to tension. The point of maximum compression indicates the diaphragm transition from plate to membrane dominant behaviours.

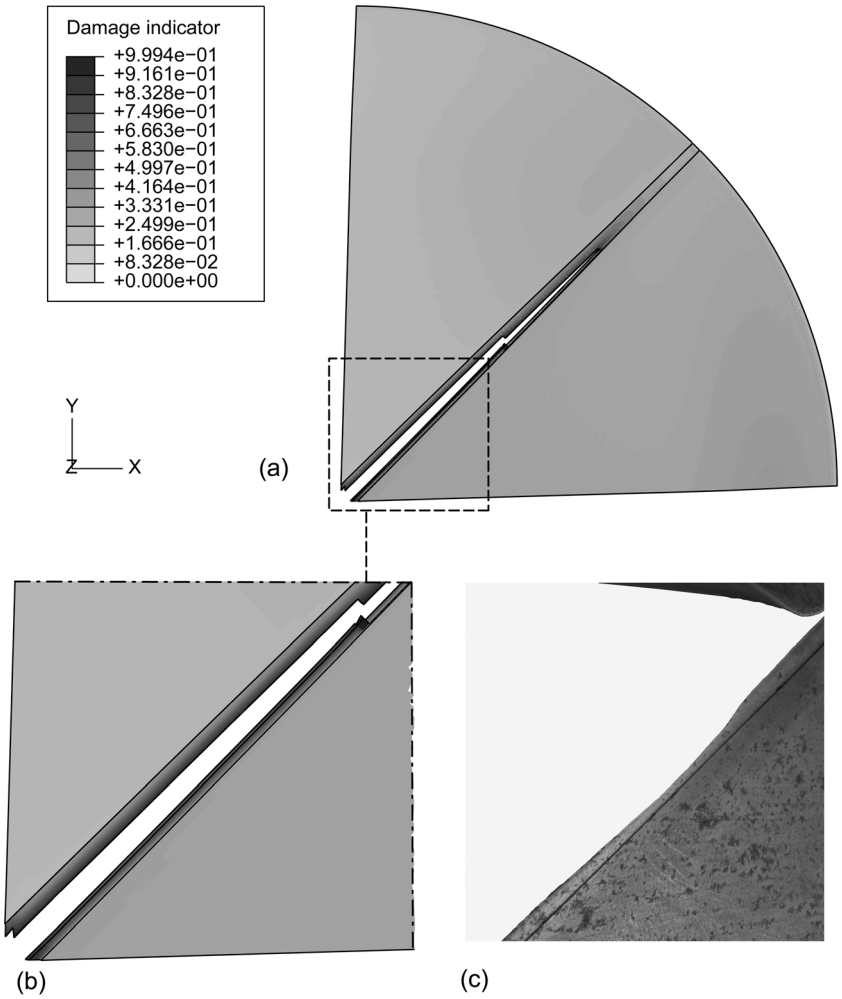

Fig. 17 Damage initiation indicator computed in diaphragm type B during tearing formation (**a**–**b**) and zoom at failure for diaphragm B2 (**c**)

Parametric Studies

In this section, the effects of two main parameters on the diaphragm burst pressure are investigated through the numerical method proposed in the previous section. The parameters investigated are the diaphragm thickness and the score depth—thickness ratio. Diaphragm thickness and score depth are indicated as t and i, respectively. The groove width is considered as constant in this parametric study since it depends on the end mill cutter mounted on the milling machine used for the specimen preparation. Table 4 summarizes the geometrical characteristics of the diaphragms analysed in the numerical parametric study.

Burst pressure vs diaphragm thickness curves for different i/t values (0.2, 0.4 and 0.7) are derived and shown in Fig. 26. For a given i/t value, diaphragm with higher thickness are characterized by a higher burst pressure. Figure 26 shows a quite linear proportionality, for a fixed i/t value, between the diaphragm thickness and the burst pressure.

Burst pressure vs score depth—thickness ratio curves for t equal to 2, 4, 6 and 8 mm are shown in Fig. 27. As the i/t value increases (for a given diaphragm thickness), the burst pressure decreases. For diaphragms with i/t values larger than 0.4, a marked linearity between i/t and the burst pressure is observable. The deviation from the linearity can be explained as follows.

All the diaphragms with score depth—thickness ratio equal to 0.2 are characterized by a failure mechanism different from that described in Figs. 16 and 17. In these diaphragms the failure does not occur in the central region of the diaphragm at the intersection of the grooves and propagates along the grooves, but it occurs along the fixed edge on the non-scored side of the diaphragm. This failure mechanism is characterized by high shear plastic strain close to the fixed edge and can be assumed as a shear failure in contrast with a membrane failure that characterizes all diaphragms with i/t higher than 0.4. The different failure mechanism justifies the slope change in Fig. 27 that takes place for diaphragms having i/t between 0.2 and 0.4. In this range of score depth—thickness ratio there is a transition from a failure mechanism taking place at the fixed edge on the non-scored side (i/t=0.2) to a failure mechanism that takes

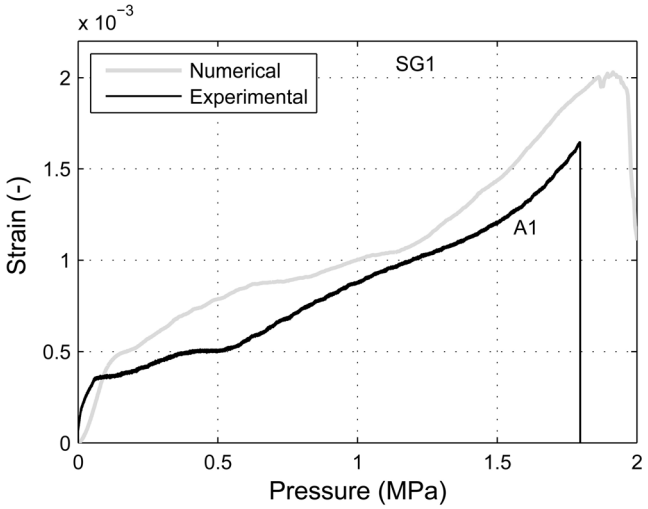

Fig. 18 Comparison of experimental and numerical strain evolution at the location SG1 for diaphragms of type A

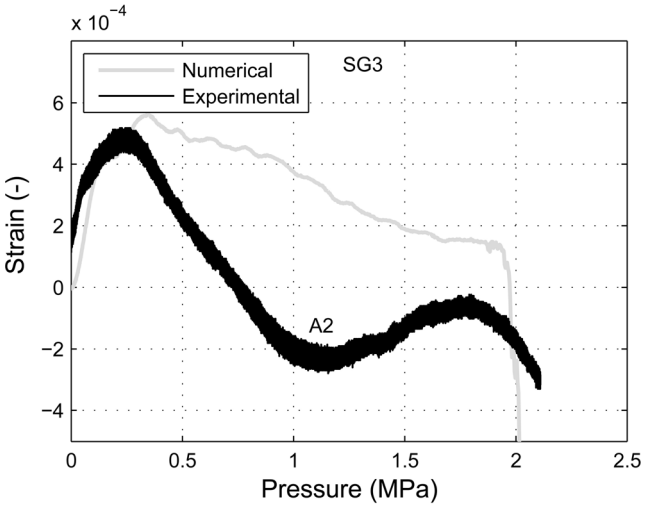

Fig. 20 Comparison of experimental and numerical strain evolution at the location SG3 for diaphragms of type A

place at the intersection of the grooves at the centre of the diaphragms (i/t=0.4).

Design Considerations

In this section, two simplified approaches for the burst pressure estimation of scored steel diaphragms are presented; the burst pressure results are compared with experimental and numerical values. The approaches herein presented are widely used by design engineers and are representative of the current design methodologies.

The first approach assumes a plate behaviour for the diaphragm and the burst pressure p_U can be determined by adopting the yield-line method [18]. Assuming the yield lines distribution proposed in Fig. 28 and, consequently, a square-base pyramidal shape collapse mechanism for the clamped edge circular plate of radius R, the internal work W_i is equal to:

$$W_i = \left(8 \cdot m_L^+ + 8 \cdot m_L^-\right)\delta \tag{11}$$

where m_L^+ and m_L^- are the positive and negative resistant bending moments per unit length for the scored and non-scored sections respectively and δ is the virtual displacement. The external work W_e due to the uniform pressure p is equal to:

$$W_e = \frac{2}{3} \cdot p \cdot R^2 \cdot \delta \tag{12}$$

The virtual work principle states that $W_i = W_e$, then the burst pressure p_U is evaluated as:

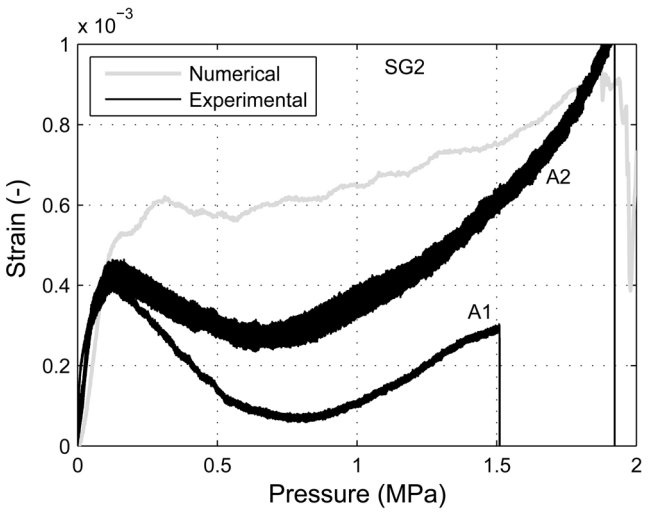

Fig. 19 Comparison of experimental and numerical strain evolution at the location SG2 for diaphragms of type A

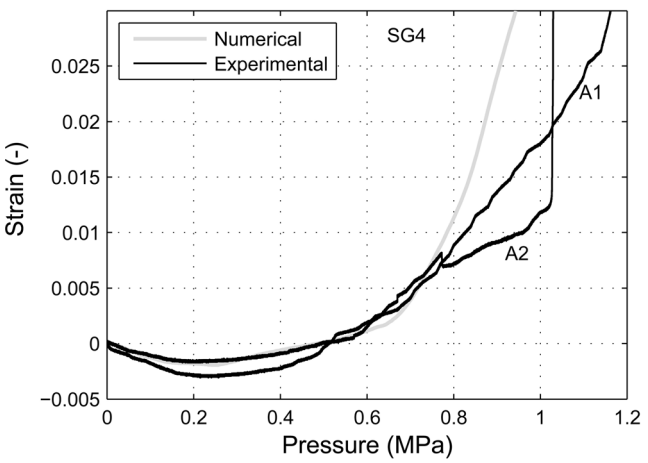

Fig. 21 Comparison of experimental and numerical strain evolution at the location SG4 for diaphragms of type A

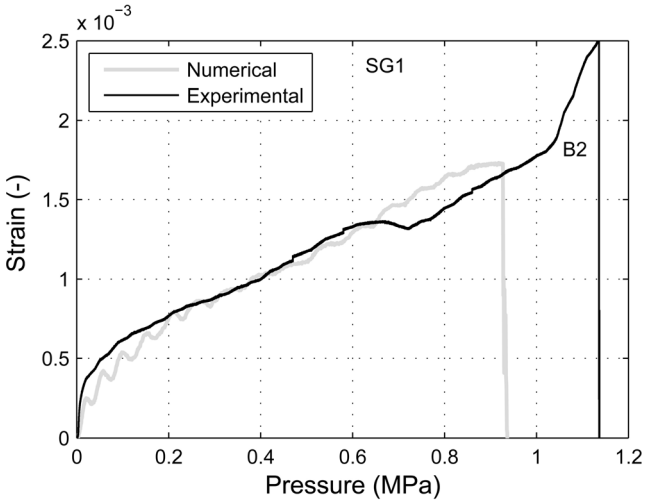

Fig. 22 Comparison of experimental and numerical strain evolution at the location SG1 for diaphragms of type B

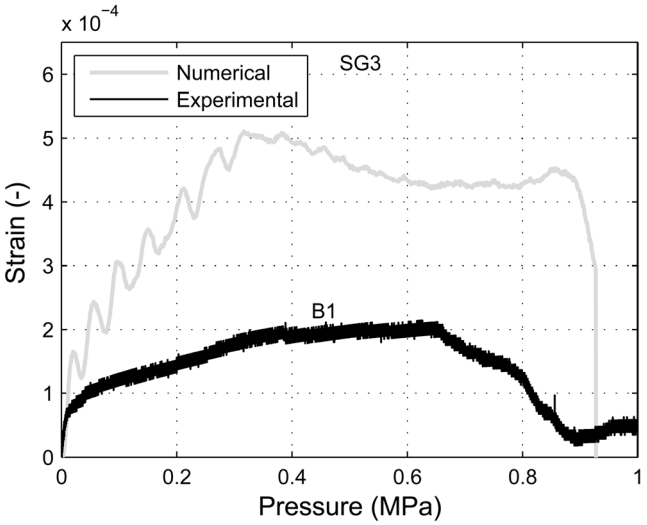

Fig. 24 Comparison of experimental and numerical strain evolution at the location SG3 for diaphragms of type B

$$p_U = \frac{3}{2}\cdot\frac{1}{R^2}\cdot\left(8\cdot m_L^+ + 8\cdot m_L^-\right) \tag{13}$$

The positive and negative plastic moments are calculated assuming a complete plastic stress distribution on the cross-section and are given by the following:

$$m_L^+ = \frac{f_{tu}\cdot h^2}{4} \qquad m_L^- = \frac{f_{tu}\cdot t^2}{4} \tag{14}$$

where f_{tu} is the steel ultimate strength, while t and h are respectively the diaphragm thickness and the difference between the thickness and the score depth. The ultimate strength f_{tu} is assumed as the average between the two experimental tests presented in Diaphragm Geometry and Material sect. and is equal to 418 MPa. The ultimate burst pressures for diaphragms type A and B according to this method are equal to 0.47 MPa and to 0.12 MPa, respectively.

In the second approach the diaphragms are considered as a flexible membrane in which the bending resistance is neglected and the deflection may become very large if compared to the plate thickness. The governing equations and the complete treatment can be found in [19], while here the elastic tensile stress at the centre of the membrane is only recalled:

$$(\sigma_r)_{r=0} = 0.423\sqrt[3]{\frac{E\cdot p^2\cdot R^2}{h^2}} \tag{15}$$

The burst pressure for both diaphragm typologies can be easily derived from equation (15) assuming $(\sigma_r)_{r=0}=f_{tu}$ and

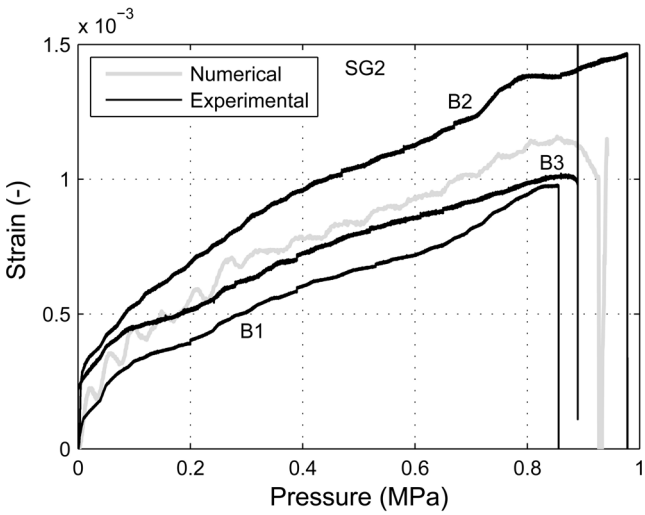

Fig. 23 Comparison of experimental and numerical strain evolution at the location SG2 for diaphragms of type B

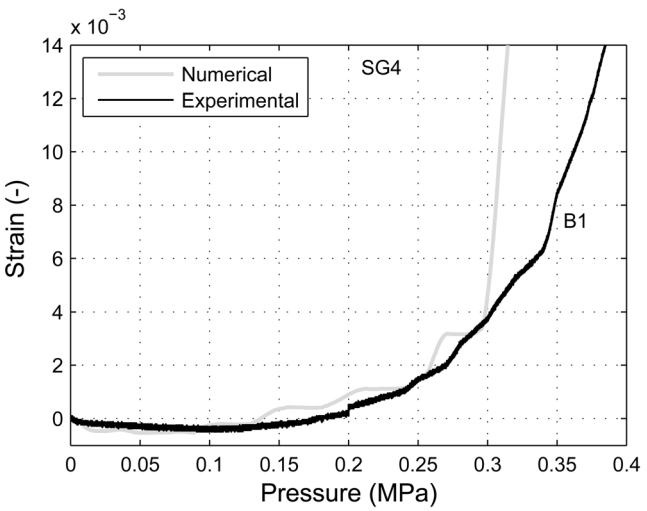

Fig. 25 Comparison of experimental and numerical strain evolution at the location SG4 for diaphragms of type B

Table 4 Diaphragms analysed in the numerical parametric study (diaphragms in italics are also considered in the experimental investigation)

Thickness (t) [mm]	Ligament [mm]	Score depth (i) [mm]	i/t [−]	Burst pressure [MPa]
2	1.6	0.4	0.2	1.80
2	*1.2*	*0.8*	*0.4*	*0.93*
2	0.6	1.4	0.7	0.44
4	3.2	0.8	0.2	3.27
4	*2.4*	*1.6*	*0.4*	*1.98*
4	1.2	2.8	0.7	1.02
4	0.6	3.4	0.85	0.56
6	4.8	1.2	0.2	5.07
6	3.6	2.4	0.4	3.20
6	2.4	3.6	0.6	2.16
6	1.8	4.2	0.7	1.65
6	1.2	4.8	0.8	1.19
6	0.6	5.4	0.9	0.88
8	6.4	1.6	0.2	6.29
8	4.8	3.2	0.4	4.13
8	3.6	4.4	0.55	3.13
8	2.4	5.6	0.7	2.25
8	1.2	6.8	0.85	1.59
8	0.6	7.4	0.925	1.14

are equal to 0.68 MPa and to 0.34 MPa for diaphragms type A and B, respectively.

Also considering a membrane mechanism just within the square generated by the negative yield lines (Fig. 28), the maximum tensile stress at the diaphragm centre is given by:

$$\sigma = 0.396 \sqrt[3]{\frac{E \cdot p^2 \cdot \left(\sqrt{2}R/2\right)^2}{h^2}} \tag{16}$$

which provides ultimate burst pressures for diaphragms type A and B equal to 1.05 MPa and to 0.53 MPa, respectively.

The comparison between the experimental burst pressures and those obtained by the methods afore illustrated, points out the limitations of the design approaches herein considered. In fact, both approaches grossly underestimate the experimental burst pressure with a better estimation for the membrane-based method. The large difference between the experimental results and these design predictions is first of all due to the assumption to consider as constant thickness the ligament length, furthermore it seems to be due to the large plastic internal work done by the diaphragm before reaching the failure. Such plastic internal work derives by the fact that all the regions of the diaphragm reach yielding; in particular the transition from

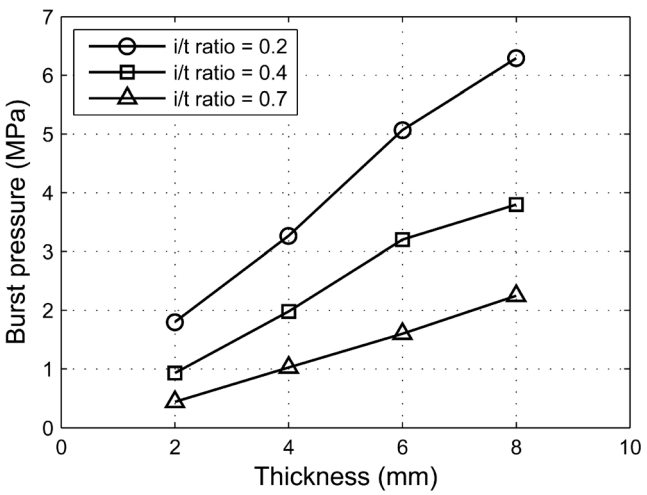

Fig. 26 Burst pressure vs diaphragm thickness for several score depth—thickness ratio (i = score depth; t = diaphragm thickness)

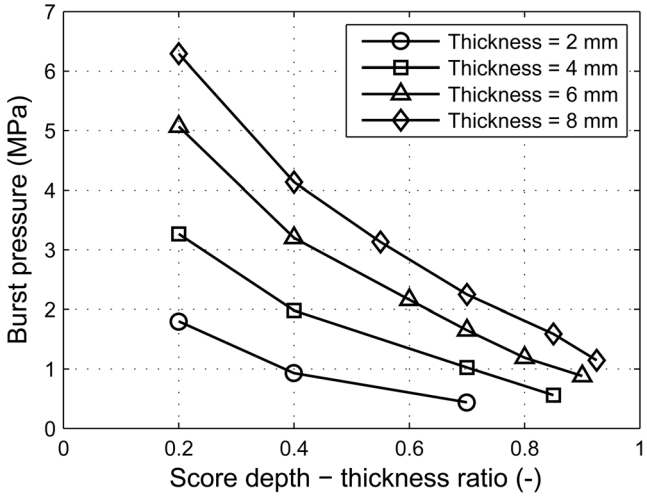

Fig. 27 Burst pressure vs score depth—thickness ratio for several diaphragm thickness

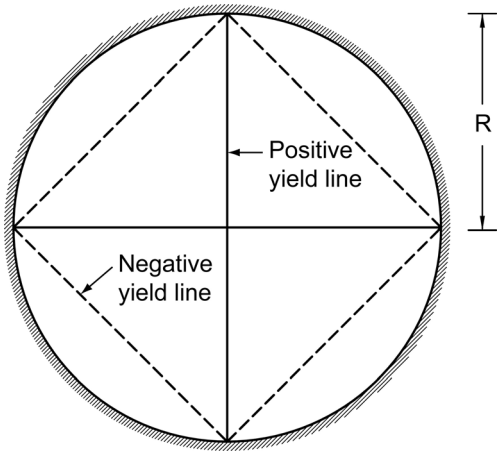

Fig. 28 Yield lines for a square-base pyramidal shape collapse mechanism

plate to membrane regime is guaranteed both by the formation of the negative plastic hinges along the clamped edge and by the yielding of the whole petal region that allows the formation of the curved deformed shape typical of the ultimate membrane regime. The large internal work brings to a high external work and therefore to large displacement and high pressure. The lack of specific design methods for taking into account the contribution of such plastic work, makes the numerical procedure here presented an important tool to have a reliable prediction of the diaphragm burst pressure.

Once assessed the reliability of the numerical procedure in the prediction of the burst pressure of scored steel diaphragms, it is important to focus our attention on the geometric and material uncertainties. Regarding the geometric uncertainty, the meshes adopted in the model are not enough refined to give us a reliable answer when the geometrical tolerance of the plate and the machining tolerance are taken into account. It is worth noting that the models adopted are characterized by a high computational cost due to the large total number of elements (355,288 and 138,898 for diaphragms types A and B, respectively) which very small size influences the time step. For this reason only the mechanical uncertainty is discussed in the following.

The variability of the material mechanical properties is referred to steel within the same class. Looking for instance to steel S235 JR, here considered, standards [8] propose an ultimate tensile strength f_{tu} ranging from 360 MPa to 510 MPa. Running two different simulations of diaphragm type B ("1° Refinement" mesh) with constitutive laws characterized respectively by the two limits of ultimate tensile strength, it is possible to observe that the burst pressure range between 0.79 MPa and 1.15 MPa for minimum and maximum f_{tu} values.

It is worth noting that the constitutive laws adopted in these simulations are obtained from a rigid vertical translation of the one presented in Fig. 4 moving the f_{tu} point respectively to the minimum and to the maximum value. The large difference in the burst pressure raised from the variation of the tensile strength, suggests that a proper mechanical identification of the material used is an important point in order to have a precise prediction of the burst pressure.

Conclusions

This paper describes the experimental results of scored circular steel diaphragms taken to failure by increasing the applied pressure. Particular attention is devoted to the tuning of the experimental set-up. The development of the numerical models and the simulations of their nonlinear response are also described.

The reliability of the proposed models to predict the experimental response is demonstrated by the good agreement of the blind prediction results with the measured data. This comparison covered global and local response indicators: global response is investigated by monitoring the burst pressures, while local response is analysed through the strain evolution at different locations. The experimental burst pressures are well predicted by the models: the maximum error found on the burst pressures is equal to −12.4 %. The evolution of the diaphragms response is predicted quite well by the models, as confirmed through the comparison of numerical and experimental strains. The assumption of perfect symmetry in the models, without the introduction of any defect or statistical variability, prevented the models from capturing the precise evolution of the strains SG2 and SG3 in type A diaphragms which is influenced by an asymmetrical failure shape. The importance of the numerical procedure presented is highlighted by the lack of simple design methods to provide a reliable prediction of the burst pressure.

Experimental and numerical results indicate that diaphragms with higher thickness are characterized by a more unstable tearing propagation which leads to asymmetric deformed shapes at failure. This asymmetry in the failure mechanism is undesirable both for diaphragms used as rupture disc in safety device applications and for diaphragms used as critical device in shock tube facilities. The parametric study carried out has also pointed out as for diaphragms with a score depth—thickness ratio larger than 0.4 the bursting pressure is linearly affected by the score depth—thickness ratio for an assigned thickness; on the contrary diaphragms with score depth – thickness ratio lower than 0.4 exhibit a failure that occurs along the fixed edge without the formation of petals. This failure mechanism is likewise undesirable for both the scored diaphragms applications.

Acknowledgments The research was financially supported by European INTERREG IT/CH 2006_2013 project ACCIDENT ID 7629770, Measure 2.2.

References

1. Nurick GN, Martin JB (1989) Deformation of thin plates subjected to impulsive loading—a review; part I—theoretical considerations. Int J Impact Eng 8:159–170
2. Nurick GN, Martin JB (1989) Deformation of thin plates subjected to impulsive loading—a review; part II—experimental studies. Int J Impact Eng 8:171–186
3. Teeling-Smith RG, Nurick GN (1991) The deformation and tearing of thin circular plates subjected to impulsive loads. Int J Impact Eng 11:77–91
4. Wright JK (1961) Shock tubes. Wiley, New York
5. Rothkopf EM, Low W (1974) Diaphragm opening process in shock tubes. Phys Fluids 17:1169–1173
6. Hickman RS, Farrar LC, Kyser JB (1975) Behavior of burst diaphragms in shock tubes. Phys Fluids 18:1249–1252
7. Colombo M, di Prisco M, Martinelli P (2011) A new shock tube facility for tunnel safety. Exp Mech 51:1143–1154
8. UNI EN 10025-2 (2005) Hot rolled products of structural steels Part 2: technical delivery conditions for non-alloy structural steels. European Committee for Standardization, Bruxelles, Belgium
9. UNI EN ISO 6892-1 (2009) Metallic materials—tensile testing—part 1: method of test at room temperature. European Committee for Standardization, Bruxelles, Belgium
10. Jansen KMB (1997) Effect of pressure on electrical resistance strain gages. Exp Mech 37:245–249
11. Ajovalasit A (2005) Embedded strain gauges: effect of the stress normal to the grid. Strain 41:95–103
12. (2007) ABAQUS analysis user's manual. Version 6.7, vol. 2
13. Baker WE, Cox PA, Westine PS, Kulesz JJ, Strehlow RA (1983) Explosion hazards and evaluation. Elsevier Scientific Publishing Company, Amsterdam
14. Hancock JW, Mackenzie AC (1976) On the mechanisms of ductile failure in high-strength steels subjected to multi-axial stress-states. J Mech Phys Solids 24:147–169
15. Gunawardena SR, Jansson S, Leckie FA (1993) Modeling of anisotropic behavior of weakly bonded fiber reinforced MMC's. Acta Metall Mater 41:3147–3156
16. Fischer FD, Kolednik O, Shan GX, Rammerstorfer FG (1995) A note on calibration of ductile failure damage indicators. Int J Fract 73:345–357
17. Wasicek M, Fischer FD, Kolednik O (2008) Effect of monotonic and cyclic loading on the leaking of a shell to bottom attachment of a tank. Stahlbau 77:524–530
18. Johansen KW (1962) Yield-line theory. Cement and Concrete Association, London
19. Timoshenko S, Woinowsky-Krieger S (1959) Theory of plates and shells. McGraw-Hill, New York